HOKKAIDO UNIVERSITY

Title	Breakdown of Protective Cr-Rich Oxide Scale Formed on Heat-Resistant Steels for Superheater Tubes in a Waste Power Generation Boiler
Author(s)	Furugaki, Takashi; Takahashi, Hiromitsu; Hayashi, Shigenari
Citation	High Temperature Corrosion of Materials, 101(1), 61-78 https://doi.org/10.1007/s11085-023-10184-0
Issue Date	2024-02
Doc URL	https://hdl.handle.net/2115/93051
Rights	This version of the article has been accepted for publication, after peer review (when applicable) and is subject to Springer Nature's AM terms of use, but is not the Version of Record and does not reflect post-acceptance improvements, or any corrections. The Version of Record is available online at: http://dx.doi.org/10.1007/s11085-023-10184-0
Type	journal article
File Information	manuscript_final.pdf

Hokkaido University Collection of Scholarly and Academic Papers : HUSCAP

Breakdown of Protective Cr-rich Oxide Scale Formed on Heat-Resistant Steels for Superheater Tubes in a Waste Power Generation Boiler

Takashi Furugaki[1], Hiromitsu Takahashi[1], Shigenari Hayashi[2]

[1]Takuma Co., Ltd., 2-2-33 Kinrakuji-cho, Amagasaki, Hyogo 660-0806, Japan; furugaki@takuma.co.jp (T.F.); hiromitu@takuma.co.jp (H.T.)
[2]Faculty of Engineering, Division of Materials Science and Engineering, Hokkaido University, Kita 13 Nishi 8, Sapporo, Hokkaido 060-8628, Japan; hayashi@eng.hokudai.ac.jp (S.H.)

Corresponding author: T. Furugaki

Keywords: high-temperature corrosion, ash, alkali metal salt vapor, heat-resistant steel, Cr-rich oxide scale, breakdown

Statements and Declarations

No funding was received for conducting this study.The datasets generated during the current study are available from the corresponding author on reasonable request.
The authors declare that they have no conflict of interest.

Author Contributions

T. Furugaki, H. Takahashi, S. Hayashi: Conception and design of study. **T. Furugaki**: Acquisition of data. **T. Furugaki, S. Hayashi**: Analysis and/or interpretation of data. **T. Furugaki**: Drafting the manuscript. **T. Furugaki, S. Hayashi**: Revising the manuscript critically for important intellectual content. **H. Takahashi, S. Hayashi**: Approval of the version of the manuscript to be publish.

Abstract

The high-temperature corrosion behavior of type 310 heat-resistant steel used for superheater tubes in waste-to-energy boilers was investigated to determine the breakdown behavior of the protective Cr-rich oxide scale in the initial stages of corrosion by conducting ash-embedded corrosion tests using combustion ash collected from an actual boiler. The corrosion tests were performed in air at a specimen temperature of 460 °C and an atmospheric temperature of 685 °C. After 24 h, the specimen surfaces were entirely covered with brown corrosion products, but there was almost no mass loss. However, the corrosion mass loss increased after 60 h. After 1–12 h, the specimen surfaces were partially covered with brown corrosion products, but in other areas, the interference color or a yellow hue remained, where no breakdown had occurred. Examination of the cross-sectional microstructures of these breakdown-free areas revealed that a protective Cr-rich oxide scale was formed on the surface after 1 h of corrosion, and sodium ferrite was distributed on the surface of the Cr-rich oxide scale. Although the breakdown of the Cr-rich oxide scale was not complete, iron chloride formation occurred at the substrate subsurface under the Cr-rich oxide scale, and the latter was partially exfoliated from the substrate in SUS310S. Cl_2 gas was also generated during the formation of sodium chromate. Therefore, despite the protective nature of the Cr-rich oxide scale, partial formation of chromate may cause chloride formation on the substrate followed by exfoliation of the scale. After scale breakdown, the Cl_2 gas caused intergranular or localized internal corrosion, and when the internal corrosion had spread to some extent, the Cr-rich oxide scale was formed again. This cycle led to the corrosion of the heat-resistant steel.

Introduction

The superheater tubes of waste-to-energy (WTE) boilers are exposed to very harsh environments that contain various corrosive gas species produced by the incineration of waste at high temperature. In addition, combustion ash containing alkali metal chlorides and heavy metal chlorides is always deposited on the surfaces of the superheater tubes, which also accelerates the surface recession of steels by high-temperature corrosion. Type 310 heat-resistant steel, which exhibits good corrosion resistance, is currently widely used for superheater tubes.

In our previous study, the effect of temperature gradients in the deposited ash on the corrosion behavior of two austenitic heat-resistant steels, namely, SUS310S and QSX5, was investigated by using the actual combustion ash obtained from a commercial WTE boiler [1]. The corrosion mass loss after 100 h at a specimen temperature of 460 °C with a temperature gradient in the deposited ash was found to be much greater than that under isothermal conditions. Both steels had formed a thin oxide scale under the isothermal conditions at 460 °C after 100 h, whereas a thick duplex oxide scale comprising an outer porous Fe-rich oxide and an inner multilayered Cr-rich oxide was generated under the temperature gradient conditions. Sodium was also detected in the inner multilayered oxide scale along with the Cr-rich oxide layers. X-ray diffraction (XRD) analysis confirmed the presence of sodium chromate, which indicated that the alkali metal chloride vapor reacted with the protective Cr-rich oxide scale to afford alkali metal chromates. This formation of alkali metal chromates by the reaction of alkali metal salt vapor with the protective Cr-rich oxide layer was considered to be the main reason for the breakdown of the Cr-rich oxide scale. In the presence of a temperature gradient, the flux of the alkali metal chloride vapor toward the specimen should be greater owing to the higher driving force for gas-phase diffusion due to the higher vapor pressure of the alkali metal chlorides near the deposit surface compared with the specimen surface, thus accelerating the breakdown of the Cr-rich oxide scale. However, in our previous study, the early-stage corrosion behavior was not investigated in detail.

The high-temperature corrosion behavior of heat-resistant steels often comprises two distinct stages: an initial incubation stage characterized by a protective effect, during which the corrosion rate is relatively slow, and a subsequent propagation (nonprotective) stage, during which the corrosion proceeds at a higher rate [2]. The breakdown of a protective oxide scale is one of the main factors precipitating this transition and the reaction of protective oxide scales with alkali metal salts has been investigated [3–11]. However, besides chromate formation, there may be another mechanism responsible for the breakdown of the protective oxide scale. In this study, the breakdown behavior of a Cr-rich oxide scale was examined.

Experimental Procedures

Specimen Preparation

The corrosion tests were performed using sections cut from commercial austenitic heat-resistant SUS310S and QSX5 steel tubes with dimensions of 10 mm × 10 mm × 1 mm. All specimen surfaces were polished with SiC paper to 4000 grit and then finished with 3 μm diamond paste. Prior to the corrosion tests, the specimens were degreased by ultrasonication in acetone for 10 min. The nominal compositions of the heat-resistant steels are shown in Table 1.

Combustion Ash

Tube side deposit ash [1] was used in this study. The ash composition analyzed by X-ray fluorescence (XRF) is shown in Table 2. The melting point of the ash was determined to be 519 °C by thermogravimetry/differential thermal analysis.

Corrosion Tests

Non-isothermal corrosion tests (i.e., with a temperature gradient in the deposit ash) were conducted in a horizontal tube furnace in air as described elsewhere [1]. The specimens were embedded in the combustion ash at a depth of 10 mm from the ash surface in a specimen holder. During the corrosion tests, the atmospheric temperature was set to 685 °C and the specimen temperature was maintained at 460 °C by cooling the specimen holder with a stream of steam. The specimen temperature of 460 °C was selected because the maximum steam temperature is 450 °C in some WTE plants, and the surface temperature of the superheater tubes is expected to be slightly higher. The temperatures of the reaction tube and specimen holder were monitored using thermocouples. The corrosion tests were conducted for various durations (1, 12, 24, 60, and 100 h).

Two specimens of each type of steel, for observation of the corrosion products and measurement of the mass change, were always used in the corrosion tests. After each corrosion test, the corrosion products formed on one of the two specimens were removed by chemical treatment according to ISO 17248:2015(E), as shown in Table 3. The mass loss of this specimen was then calculated based on the measured masses before corrosion and after the removal of the oxide scale/corrosion products. The other specimen was mounted in epoxy resin and cut and polished under oil to prevent dissolution of the reaction products in water. The detailed microstructures of the corrosion products were examined by scanning electron microscopy (SEM; JEOL JSM-IT200).

After corrosion for 1 or 12 h, the specimens were thinned using a focused ion beam (FIB; Hitachi FB-2100) at an accelerating voltage of 10 kV. Cross-sectional scanning transmission electron microscopy (STEM; Hitachi HD-2000) images were then recorded using an accelerating voltage of 200 kV. Energy-dispersive X-ray spectroscopy (EDS) was also used to examine the oxide scale formed in the early stage of corrosion.

Results

Surface Morphology of Corroded Specimens

The appearances of the specimens after corrosion for 1, 12, 24, 60, and 100 h are presented in Fig. 1 (the images after 100 h were adapted from Ref. [1]). The arrows in Fig. 1 indicate the positions of the metal nails used to mount the specimens on the specimen holder, which were in contact with the specimen surface. Although it is difficult to judge from the images in Fig. 1, the interference color still remained on the surfaces of both the SUS310S and QSX5 specimens after 1 h of corrosion, but some areas were covered by brown corrosion products. These brown corrosion products covered a greater area on the SUS310S specimen than on the QSX5 specimen. After 12 or 24 h of corrosion, most of the surface was covered by bright brown corrosion products for both the SUS310S and QSX5 specimens. Following corrosion for 60 or 100 h, the surfaces of the steel specimens had become

very rough and were covered by bright brown and dark brown corrosion products [1]. In addition, yellow and green reaction products were observed with the combustion ash after 100 h. The combustion ash, which was white in color, was also found to be partially adhered to the corrosion products for most of the specimens.

Corrosion Kinetics

The corrosion kinetics of the steel specimens are plotted in Fig. 2. The corrosion mass loss remained minimal for at least 24 h then increased over time, indicating that the transition from the incubation stage to the propagation stage occurred between 24 and 60 h for both steels. The corrosion rate of SUS310S in the propagation (nonprotective) stage after scale breakdown was much higher than that of QSX5.

Surface Morphology and Elemental Distributions after 1 and 12 h of Corrosion

Figures 3 and 4 show the surface morphologies and EDS elemental distribution maps of areas where no thick layer of corrosion products was observed after corrosion for 1 and 12 h, respectively. After 1 h of corrosion, the specimen surfaces were smooth, and the deposition of salt particles with dark contrast was observed on the steel surfaces. The homogeneous distributions of Cr, Fe, and Ni suggested that a thin oxide scale was formed on these areas. After 12 h of corrosion, the smooth areas on both specimen surfaces were still covered by a relatively thin oxide scale, but the surfaces were also partially coated with iron and chromium chlorides as indicated by the arrows in Fig. 4.

Cross-sectional Microstructures after 1 and 12 h of Corrosion

Cross-sectional STEM images of the steel specimens after 1 h of corrosion are presented in Fig. 5. A thin continuous oxide scale of approximately 30–50 nm thickness was formed on both SUS310S and QSX5. This oxide scale was well adhered to the substrate in both cases.

The cross-sectional STEM images of the specimens after 12 h of corrosion are shown in Fig. 6. A thick oxide layer was formed locally on the SUS310S specimen. This was found to be a duplex scale composed of an outer dense oxide layer and an inner porous oxide layer. The thickness of the oxide scale formed on QSX5 was not uniform, and penetration of the outer oxide layer into the deposit ash was observed. This oxide scale consisted of a dense outer oxide layer and a thin inner layer.

Cross-sectional Elemental Distribution Maps after 1 and 12 h of Corrosion

The distributions of each element in the oxide scale formed on SUS310S after 1 h of corrosion are shown in Fig. 7. These EDS mapping results confirmed the outer and inner layers to be composed of Fe-rich and Cr-rich oxides, respectively. Na was uniformly distributed in the outer Fe-rich oxide layer. Ca and Cl were also detected in the Fe-rich oxide layer, but neither Cl nor S was detected in the oxide scale, suggesting the formation of sodium ferrite, $NaFe_2O_3$, below the calcium chloride layer. Figure 8 shows the elemental distribution maps of the oxide scale formed on QSX5 after 1 h of corrosion. The structure of the oxide scale

was the same as that formed on SUS310S, but the signal from Fe was considerably weaker. Na was also detected on the surface of the oxide scale, suggesting the formation of $NaFe_2O_3$ and/or $NaCr_2O_4$. Ca and Cl derived from the ash were also detected on the surface of the oxide scale, although no penetration of Cl and S into the substrate was observed after 1 h of corrosion.

The elemental distribution maps for SUS310S after 12 h of corrosion are presented in Fig. 9. The outer dense oxide layer was iron oxide. Beneath this layer was a thin inner Cr-rich oxide layer. The porous inner scale was composed of Fe, O, and Cl, suggesting the formation of iron chlorides. Ni was not detected within the oxide layer but it was enriched in the subsurface region just below the inner Fe-rich oxide/chloride. The ash components Ca and K were not detected in the oxide scale, but Na was identified on the surface of the oxide scale in the Fe-rich oxide layer. Si appeared to be distributed just below the dense, continuous chromium oxide layer. Na was also detected in the W deposition with intensity comparable to that in the Fe-rich oxide scale because the energy of the Lα line of Ga (=1.098 keV), which was used in the FIB process, is close to that of the Na Lα line (=1.012 keV). Si was also detected in the W deposition owing to the similar energies of the Si Kα line (=1.739 keV) and W Mα line (=1.774 keV).

Figure 10 shows the elemental distribution maps of the oxide scale formed on QSX5 after corrosion for 12 h. The oxide scale had a triplex structure composed of an outer Fe-rich oxide layer, a thin inner Cr-rich oxide layer, and a very thin innermost Si-rich oxide layer. Na was also detected in the Fe-rich oxide layer. Although Cl was detected at the scale/steel interface, the formation of iron chlorides was not observed in this mapping analysis. Ni was consistently enriched on the substrate surface.

Cross-sectional Observations after 24, 60, and 100 h of Corrosion

Cross-sectional microstructures after 24, 60, and 100 h of corrosion are shown in Fig. 11 (the images after 100 h were adapted from Ref. [1]). Both steels displayed a thin uniform oxide scale after corrosion for 24 h, which had partially exfoliated from the substrate. In addition, internal corrosion attacks had occurred along the grain boundaries in some areas for both steels. However, the internal corrosion of the QSX5 specimen was less pronounced than that of the SUS310S specimen. A very porous outer scale incorporating the ash had formed on the thin oxide scale in the areas where internal corrosion attack had occurred. After 60 h of corrosion, the scales formed on both steels displayed a duplex structure consisting of an outer porous layer and an inner thin layer, similar to those formed after 100 h of corrosion. A thick inner layer was formed in some areas on both steels, but this layer was thinner in the case of QSX5. In both steels, further evidence for internal corrosion attacks along the grain boundaries was observed beneath the inner scale. Although the depth of intergranular corrosion after 60 h was greater than that after 24 h, there was no further development of intergranular corrosion after 100 h. Both steels had undergone severe attack after 100 h of corrosion, with the formation of an inner multilayer structure consisting of Fe-rich and Cr-rich oxide layers. A porous outer Fe-rich oxide layer incorporating ash components was observed. As mentioned earlier, in our previous study we detected some Na in the inner scale along with chromium oxide, suggesting the formation of sodium chromate, which was confirmed by XRD.

Elemental Distribution Maps of Internal Corrosion after 24 h of Corrosion

Elemental distribution maps of the internal corrosion regions of SUS310S after 24 h are shown in Fig. 12. The porous outer scale

was composed of Fe, Cr, and O, suggesting the formation of iron and chromium chlorides. The Cr-rich oxide scale remained on the original substrate surface. Ni metal and chromium oxide were distributed in the internal corrosion regions below the Cr-rich oxide scale. Among the ash components, Na, S, and Ca were distributed in the outer scale, while Cl was distributed in the outer scale and internal corrosion regions. Figure 13 shows the elemental distribution maps of the internal corrosion regions of QSX5 after 24 h. Cr-rich oxide with dark contrast was observed as an internal corrosion product. The ash components Ca, Na, K, and Cl were detected on the substrate surface but not at the tip of the internal corrosion region. Silicon oxide was observed on the surface of the substrate and within the internal corrosion region.

Discussion

Both SUS310S and QSX5 can form a protective Cr-rich oxide scale under oxidizing atmospheres such as air or oxygen, even at relatively low temperatures of approximately 400–500 °C [12, 13]. As shown in Figs. 2–5, protection against corrosion by the formation of a Cr-rich oxide scale during the early stage of the corrosion tests was observed even though the steel specimens were embedded in combustion ash and exposed to air. This protective stage persisted for up to about 24 h for both steels before the system transitioned to the nonprotective stage of corrosion. Because the corrosion rate of the SUS310S steel in the nonprotective stage was considerably higher than that of QSX5, it is important to discuss the corrosion behavior of heat-resistant steels in the nonprotective stage under the deposit-induced condition with a temperature gradient. However, we mainly discuss the transition from the protective stage to the nonprotective stage of corrosion in the following subsections.

Breakdown of the Cr-rich Oxide Scale during the Initial Corrosion Stage

After corrosion for 1 h, both specimens had formed a thin oxide scale possessing a duplex structure. The outer layer was composed of Fe-rich oxide and Na was also detected. The inner layer consisted of Cr-rich oxide and trace amounts of Na were detected in its outer part based on STEM analysis. These results suggest that alkali metal salts in the ash, especially NaCl, reacted with the initially formed oxide layers to generate $NaFeO_2$ and/or Na_2CrO_4 according to reactions (1) and (2). Under the assumption that the initially formed Fe- and Cr-rich oxides were Fe_2O_3 and Cr_2O_3, the Gibbs free energies of formation (ΔG) for sodium ferrite ($NaFeO_2$) and sodium chromate (Na_2CrO_4) in air (P_{O2} = 0.2 atm) were calculated to be −173 and −26 kJ, respectively. In these calculations, the vapor pressure of NaCl in the combustion ash ($P_{NaCl} = 3.5 \times 10^{-9}$ atm) and chlorine potential in the atmosphere ($P_{Cl2} = 8.1 \times 10^{-9}$ atm) at 460 °C calculated by FactSage were used.

$$2Fe_2O_3(s) + 4NaCl(g) + O_2 = 4NaFeO_2(s) + 2Cl_2 \quad (1)$$

$$\Delta G^0(T = 460℃) = -335\ \text{kJ}$$

$$2/5Cr_2O_3(s) + 8/5NaCl(g) + O_2 = 4/5Na_2CrO_4(s) + 4/5Cl_2 \quad (2)$$

$$\Delta G^0(T = 460℃) = -62\ \text{kJ}$$

Thus, both products could be formed under the present conditions. However, the protective Cr-rich oxide layer still remained just above the substrate after 1 h of corrosion as shown in Fig. 5, and the corrosion progressed in the protective stage.

After prolonged corrosion for 12 h, a porous Fe-rich oxide layer was formed below the Cr-rich oxide layer on SUS310S. Cl was also detected in the former layer, suggesting the generation of iron chloride beneath the protective Cr_2O_3 layer, which indicates that salts and/or Cl_2 can penetrate as gaseous species through the Cr_2O_3 layer and/or the layers of alkali metal chromates and ferrites [1]. The formation of iron chloride below the protective Cr-rich oxide scale at 460 °C in air can be evaluated using reactions (3) and (4) under the assumption that the chlorine potential at the scale/substrate interface was the same as that in the gaseous atmosphere, $P_{Cl2} = 8.1 \times 10^{-9}$ atm; that is, the Cl_2 required for the formation of iron chloride was derived from the combustion ash.

$$\mathrm{Fe(s) + Cl_2(g) = FeCl_2(s)} \quad (3)$$

$$\mathrm{2/3Fe(s) + Cl_2(g) = 2/3FeCl_3(s)} \quad (4)$$

$$\Delta G(3) = -208\,\mathrm{kJ}$$

$$\Delta G(4) = -127\,\mathrm{kJ}$$

Thus, the Gibbs free energies of formation are negative for both reactions, which suggests that $FeCl_2$ can be formed below the protective Cr_2O_3 scale at a lower oxygen potential, which was estimated as 7×10^{-43} atm in our previous study [1]. The formation of highly volatile iron chloride species resulted in detachment of the Cr-rich oxide scale from the substrate and loss of its protective effect, i.e., scale breakdown occurred. The iron chloride was oxidized to form a porous outer iron oxide scale at the outer part of the oxide scale with higher oxygen potential after the detachment of the protective Cr_2O_3 and produced chlorine. This process is referred to as active oxidation, which accelerates the corrosion/oxidation in the nonprotective stage of corrosion.

The formation of sodium ferrite ($NaFeO_2$) and sodium chromate (Na_2CrO_4) in reactions (1) and (2) also generates Cl_2, which may contribute another source of Cl_2 to penetrate the substrate through the protective oxide scale. The calculated chlorine potentials due to chromate formation and ferrite formation were P_{Cl2}_chromate $= 3.4 \times 10^{-7}$ atm and P_{Cl2}_ferrite $= 7.2 \times 10^{-7}$ atm, respectively. These chlorine potentials produced by reactions (1) and (2) are two orders of magnitude larger than those in the atmosphere. The formation of alkali metal chromates/ferrites further promotes the generation of iron chloride species. Thus, these processes were detrimental to the protectiveness of the oxide scale because they promoted its breakdown by producing a higher chlorine potential near the surface. The superior breakdown resistance of QSX5 may be attributable to its formation of a Si-rich oxide layer as shown in Fig. 10. However, further investigation is necessary to clarify the effect of this layer on the scale breakdown behavior.

Corrosion Behavior after Transition to the Nonprotective Corrosion Stage

After 24 h of corrosion, the surfaces of both steels were covered with brown corrosion products as shown in Fig. 1. However, the mass loss of both steels remained low up to this point because the majority of the surface was still covered by the protective oxide scale (Fig. 11a). By this time point, deep but localized regions of internal corrosion had formed. These regions had become more extensive by 60 h. Above the internal corrosion regions, a thick outer porous oxide scale composed of Fe-rich oxide incorporating ash particles had also formed. Relatively strong Cl and Ni signals were detected in the internal corrosion regions, which suggested the formation of nickel chloride. The Fe and Cr in the steel evaporated as chlorides, which resulted in the enrichment of Ni in the surface of the steel. In these regions with a high Ni content, chlorination of the Ni occurred, which may have accelerated the growth of the internal corrosion regions.

The internal corrosion regions formed in QSX5 were much thinner than those in SUS310S. The formation of SiO_2 on the surface and along the grain boundary corrosion regions was observed after 24 h (Fig. 13). Ni enrichment in the subsurface region was not observed for QSX5, suggesting that the SiO_2 layer could prevent the penetration of chlorine that may have been responsible for the breakdown of the protective Cr_2O_3 scale via the formation of iron chloride.

Corrosion Evolution Diagram

Figure 14 presents a schematic diagram illustrating the breakdown of the Cr-rich oxide scale during the early stage of corrosion. After 1 h, a molten region was formed at the surface of deposit, and the alkali metal salt vapor diffused in the solid region of deposit to the specimen surface (Fig. 14a). At this point, although sodium ferrite was formed by the reaction between the Fe-rich oxide and NaCl vapor, the protective Cr-rich oxide scale remained on the specimen surface. Alongside the formation of the sodium ferrite, Cl_2 gas was generated. After 12 h of corrosion, sodium chromate also started to form via the reaction between the alkali metal salt vapor and the Cr-rich oxide scale. The Cr-rich oxide scale then became exfoliated from the steel surface following the formation and volatilization of the iron chloride (Fig. 14b). After 24 h, the protective effect of the Cr-rich oxide scale had mostly been lost owing to expansion of the exfoliated area, and further chlorination continued below the now-exfoliated Cr-rich oxide scale. The specimen was corroded by active oxidation (Fig. 14c). The Cr-rich oxide scale could then be re-formed because of the sufficiently high Cr content in the alloy subsurface region due to the Fe consumption via chlorination. The repetition of these processes allowed the corrosion to proceed.

Conclusions

The breakdown behavior of the protective Cr-rich oxide scale on heat-resistant steels embedded in combustion ash containing alkali metal chlorides during the early stage of corrosion in air was investigated. The obtained results can be summarized as follows:

1) The specimen surface featured a relatively thick layer of corrosion products after 1–12 h of corrosion, although most of the specimen surface was covered by a protective Cr-rich oxide scale. After 24 h of corrosion, a thick outer porous Fe-rich oxide scale was generated above the Cr-rich oxide scale in the areas where internal corrosion attack occurred. The internal corrosion

regions became more extensive with increasing corrosion time. The transition from the protective stage to the nonprotective stage occurred after 24 h of corrosion, and no clear difference with respect to the time needed for this transition was observed between QSX5 and SUS310S.

2) The formation of sodium ferrite and sodium chromate in the protective oxide scale was observed. However, no chlorides or sulfides were detected on the steel surfaces.

3) After 12 h of corrosion, a porous iron oxide/chloride layer was formed below the protective Cr-rich oxide scale on SUS310S. Although the formation of iron oxide/chloride was not confirmed on QSX5, Cl was detected at the scale/steel interface, suggesting that chlorine could penetrate the protective oxide scale. The formation of alkali metal ferrites and chromates increased the local Cl_2 potential, which may have further promoted the penetration of chlorine through the oxide scale. Thus, reactions between the protective oxide scale and salt vapors could be one of the factors contributing to the breakdown of the oxide scale.

4) After the breakdown of the protective Cr-rich oxide scale, an internal region of corrosion products mainly consisting of nickel chloride was formed. The area of the internal corrosion region increased over time. The effect of interactions with chlorine appeared to promote the growth rate of the inner layer. The formation of a SiO_2 layer on QSX5 may have inhibited the penetration of chlorine through the oxide scale.

Acknowledgments

This work was supported by the “Advanced Research Infrastructure for Materials and Nanotechnology in Japan (ARIM)” of the Ministry of Education, Culture, Sports, Science and Technology (MEXT). Grant Number JPMXP1223HK0023 (Hokkaido University).

References

[1] Furugaki T, Takahashi H, Hayashi S. Effect of temperature gradient in ash on high-temperature corrosion of super-heater material in a waste power generation boiler. *Oxid Met*. 2022;98:511–528.

[2] Birks N, Meier GH, Pettit FS. *Introduction to High Temperature Oxidation of Metals, 2nd Edition*. Cambridge, UK: Cambridge University Press; 2006.

[3] Phother-Simon J, Jonsson T, Liske J. Continuous KCl addition in high temperature exposures of 304 L – A way to mimic a boiler environment. *Corros Sci*. 2020;167:108511.

[4] Karlsson S, Pettersson J, Johansson L-G, et al. Alkali induced high temperature corrosion of Stainless Steel: the influence of NaCl, KCl and $CaCl_2$. *Oxid Met.* 2012;78:83–102.

[5] Pettersson J, Folkeson N, Johansson L-G, et al. The effects of KCl, K_2SO_4 and K_2CO_3 on the high temperature corrosion of a 304-type austenitic stainless steel. *Oxid Met.* 2011;76:93–109.

[6] Pettersson C, Pettersson J, Asteman H, et al. KCl-induced high temperature corrosion of the austenitic Fe–Cr–Ni alloys 304L and Sanicro 28 at 600 °C. *Corros Sci.* 2006;48:1368–78.

[7] Pettersson C, Johansson L-G, Svensson J-E. Corrosivity of KCl(g) at temperatures above its dew point - initial stages of the high temperature corrosion of alloy Sanicro 28 at 600 °C. *Mater Sci Forum*. 2006;522–523:539–546.

[8] Davidsson KO, Åmand L-E, Leckner B. Potassium, chlorine, and sulfur in ash, particles, deposits, and corrosion during wood combustion in a circulating fluidized-bed boiler. *Energy Fuels*. 2007;21:71–81.

[9] Karlsson S, Åmand L-E, Liske J. Reducing high-temperature corrosion on high-alloyed stainless steel superheaters by co-combustion of municipal sewage sludge in a fluidised bed boiler. *Fuel*. 2015;139:482–493.

[10] Eklund J, Persdotter A, Hanif I, et al. Secondary corrosion protection of FeCr(Al) model alloys at 600 °C – the influence of Cr and Al after breakaway corrosion. *Corros Sci*. 20121;189:109584.

[11] Izzuddin H, Hayashi S, Yoneda S, et al. Effect of Mo on corrosion behavior of Ni20Cr–xMo alloys in air with NaCl–KCl–$CaCl_2$ vapor at 570 °C. *Mater Corros*. 2020;71:1488–1499.

[12] Viklund P, Pettersson R. HCl-induced high temperature corrosion of stainless steels in thermal cycling conditions and the effect of preoxidation. *Oxid Met.* 2011;76:111–126.

[13] Jonsson T, Folkeson N, Halvarsson M, et al. Microstructural investigation of the HCl-induced corrosion of the austenitic alloy 310S (52Fe26Cr19Ni) at 500 °C. *Oxid Met*. 2014;81:575–596.

Caption List

Fig. 1 Surface observations of the specimens after the corrosion tests

Fig. 2 Corrosion kinetics

Fig. 3 Surface morphologies and elemental distribution maps after 1 h of corrosion: (a) SUS310S, (b) QSX5

Fig. 4 Surface morphologies and elemental distribution maps after 12 h of corrosion: (a) SUS310S, (b) QSX5

Fig. 5 STEM images after 1 h of corrosion: (a) and (b) SUS310S, (c) and (d) QSX5

Fig. 6 STEM images after 12 h of corrosion: (a) and (b) SUS310S, (c) and (d) QSX5

Fig. 7 Elemental distribution maps of SUS310S after 1 h of corrosion

Fig. 8 Elemental distribution maps of QSX5 after 1 h of corrosion

Fig. 9 Elemental distribution maps of SUS310S after 12 h of corrosion

Fig. 10 Elemental distribution maps of QSX5 after 12 h of corrosion

Fig. 11 Cross-sections after the corrosion tests: (a) and (a') SUS310S for 24 h, (b) and (b') SUS310S for 60 h, (c) SUS310S for 100 h, (d) and (d') QSX5 for 24 h, (e) and (e') QSX5 for 60 h, and (f) QSX5 for 100 h

Fig. 12 Elemental distribution maps of SUS310S after 24 h of corrosion

Fig. 13 Elemental distribution maps of QSX5 after 24 h of corrosion

Fig. 14 Schematic image of corrosion behavior before the breakdown of the protective Cr-rich oxide scale

Table List

Table 1 Chemical compositions of the superheater tube materials

Table 2 Tube side ash composition determined by XRF

Table 3 Chemical treatment procedure based on ISO 17428:2015(E)

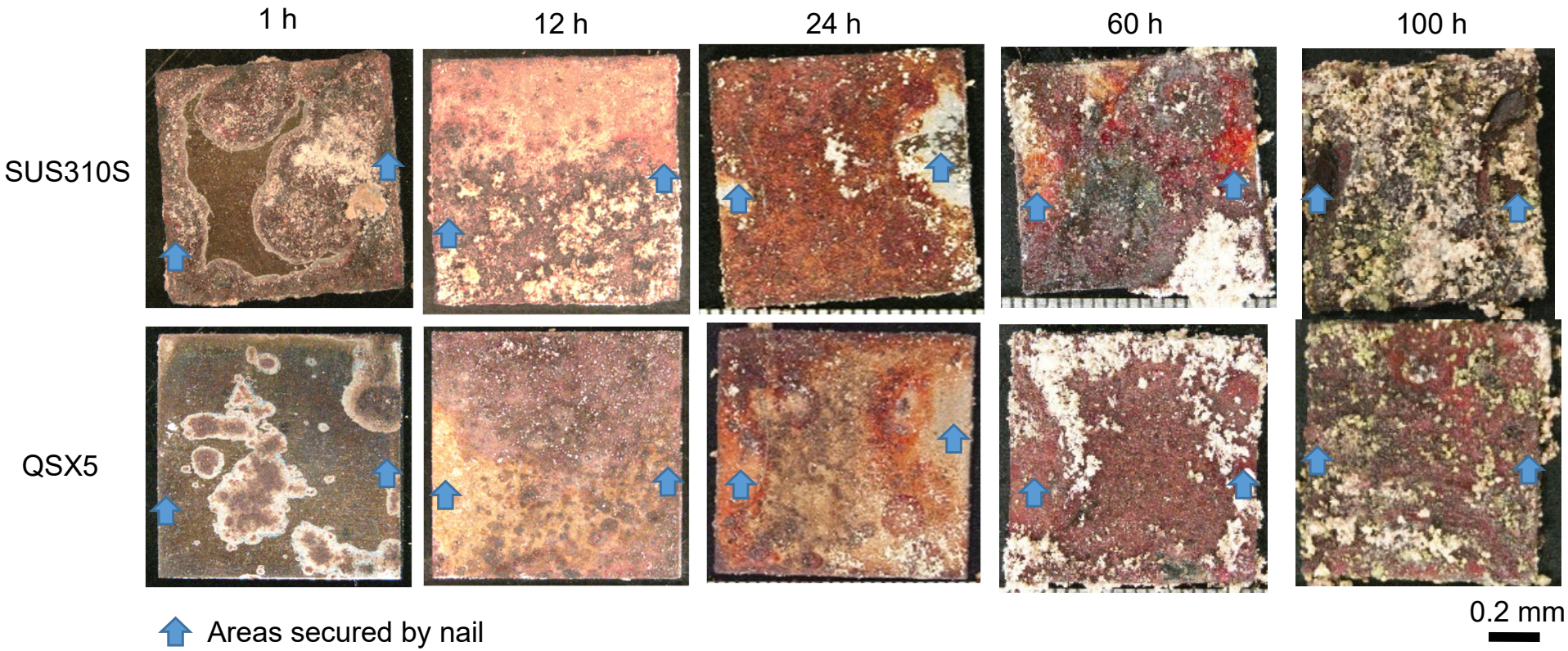


Fig. 1 Surface observations of the specimens after the corrosion tests

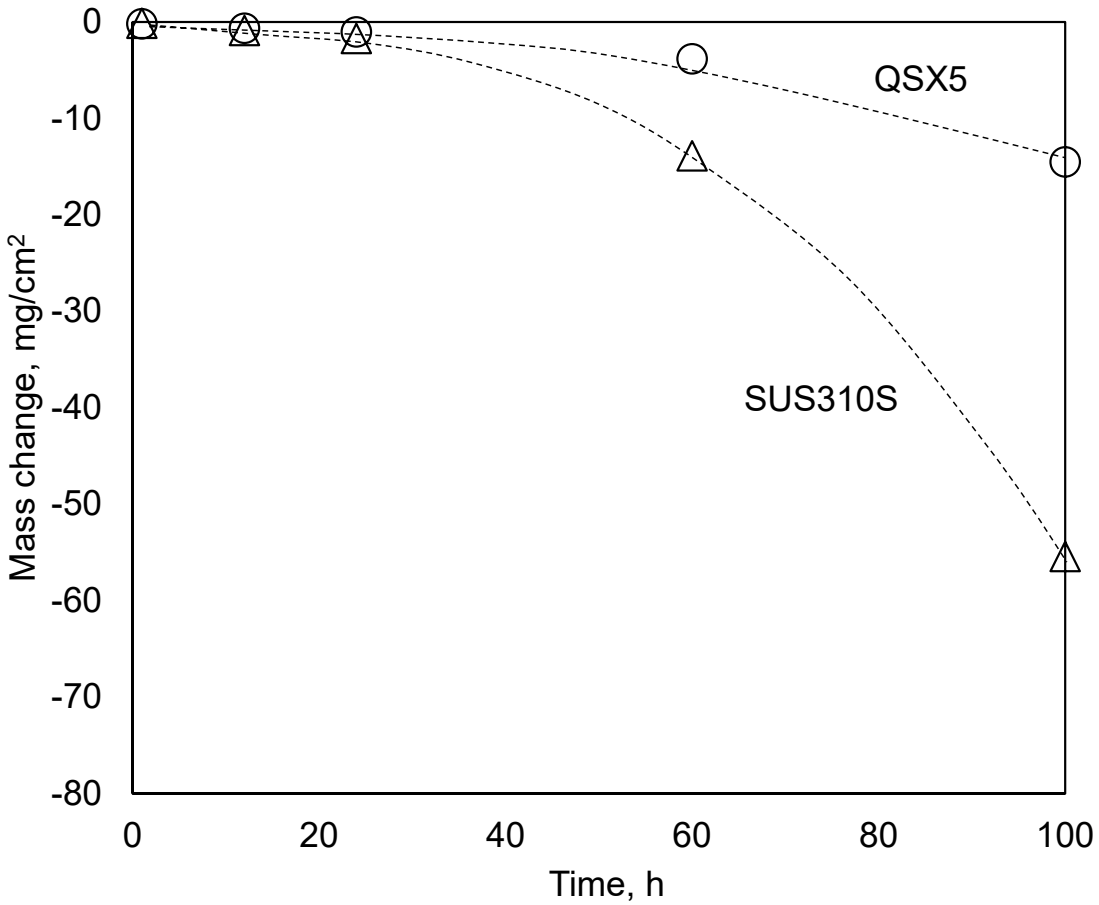


Fig. 2 Corrosion kinetics

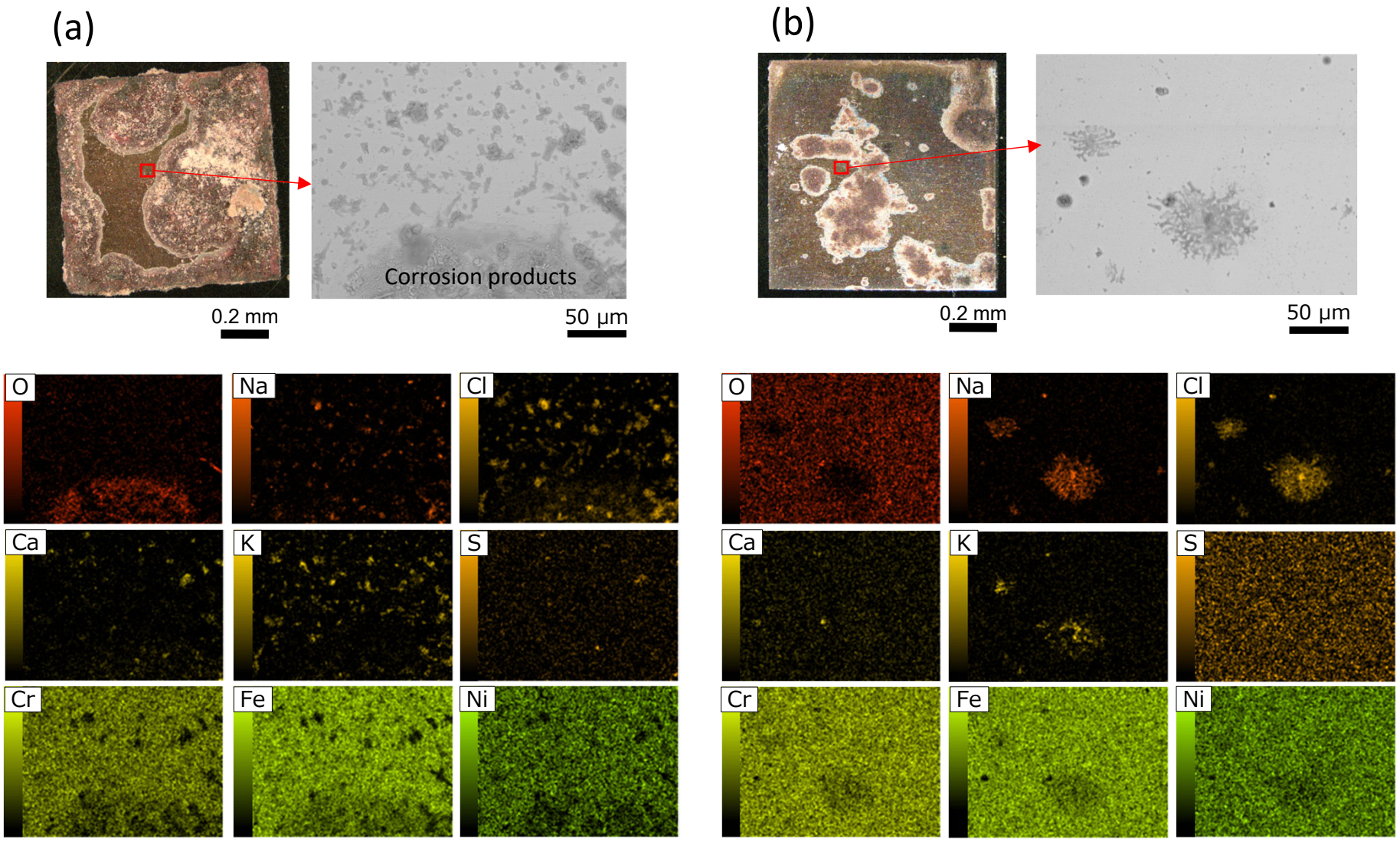


Fig. 3 Surface morphologies and elemental distribution maps after 1 h of corrosion:(a) SUS310S, (b) QSX5

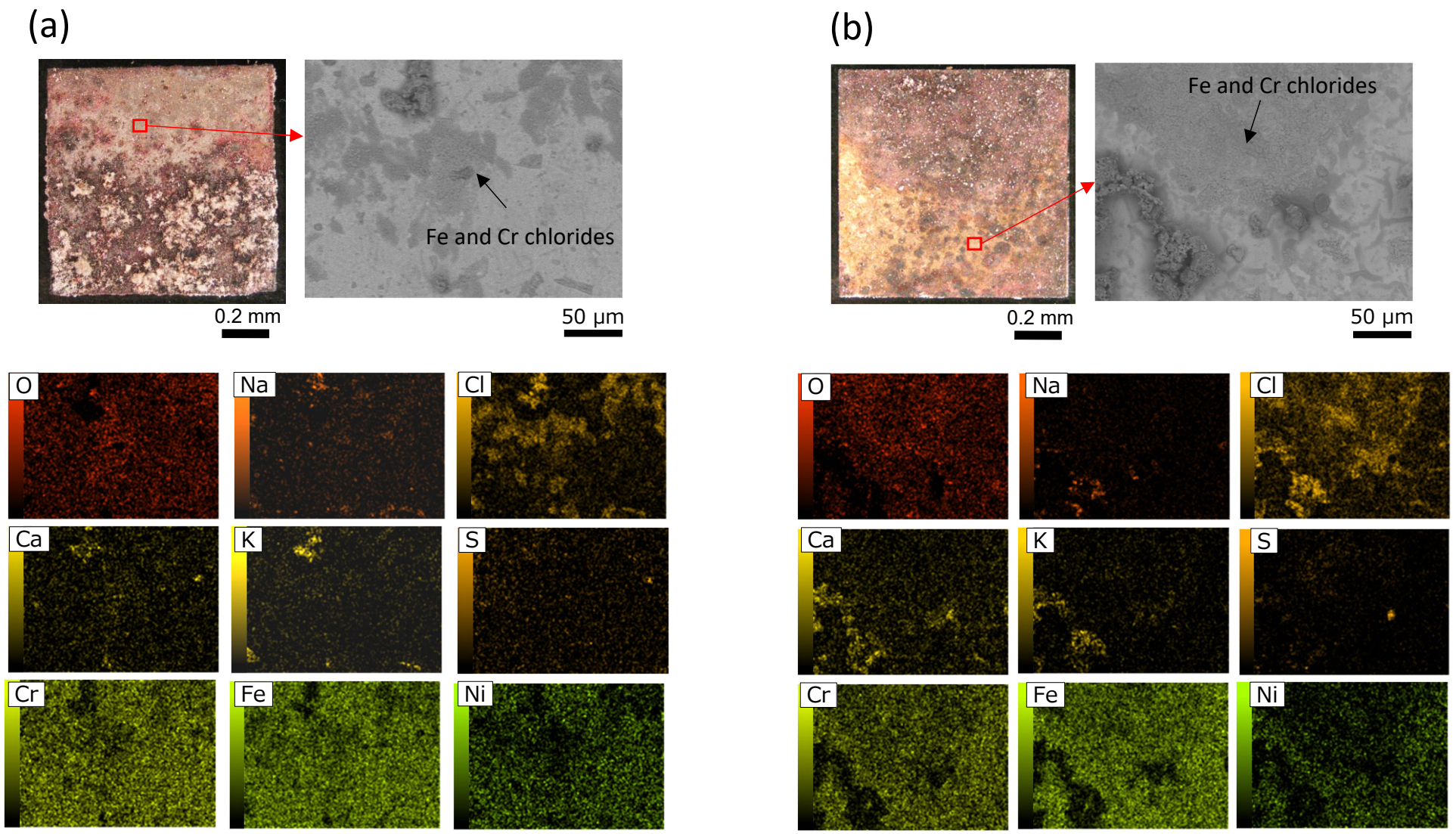


Fig. 4 Surface morphologies and elemental distribution maps after 12 h of corrosion: (a) SUS310S, (b) QSX5

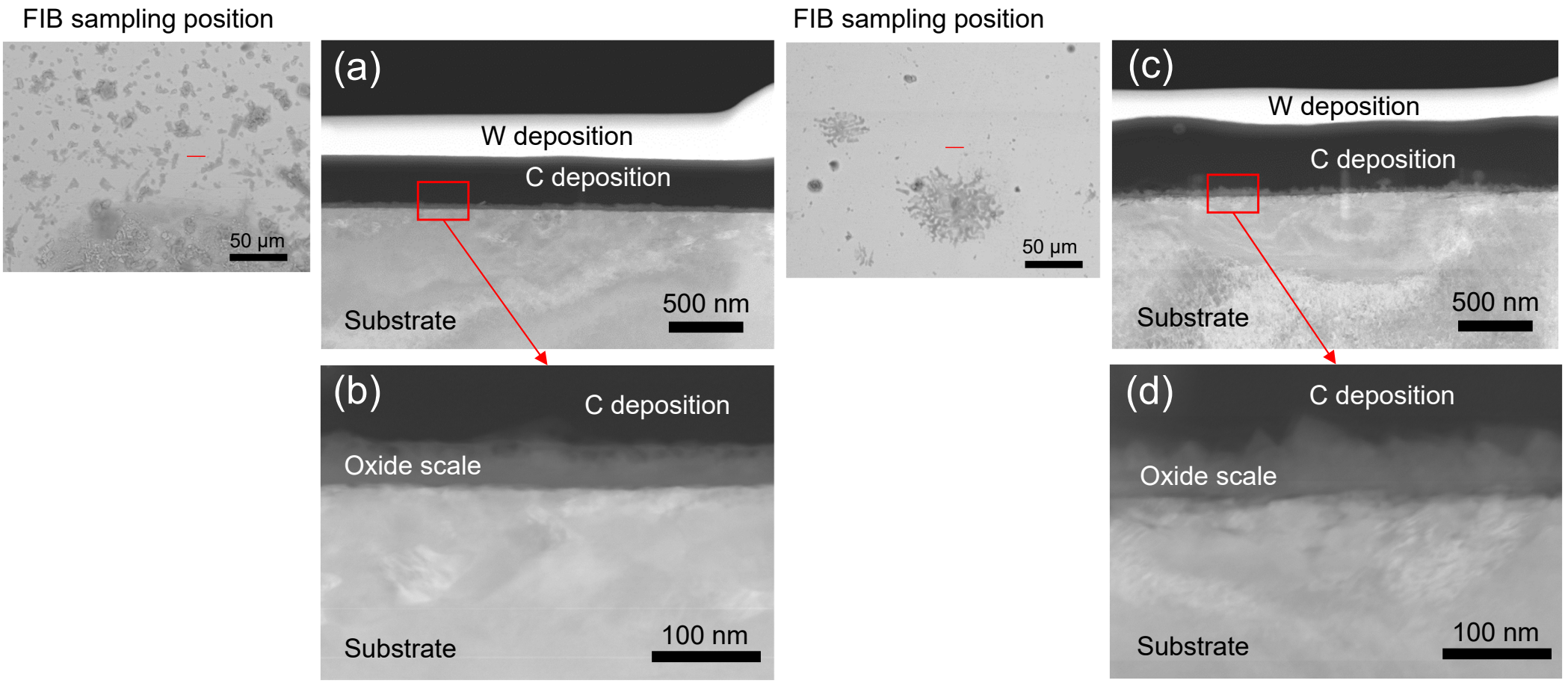


Fig. 5 STEM images after 1 h of corrosion: (a) and (b) SUS310S, (c) and (d) QSX5

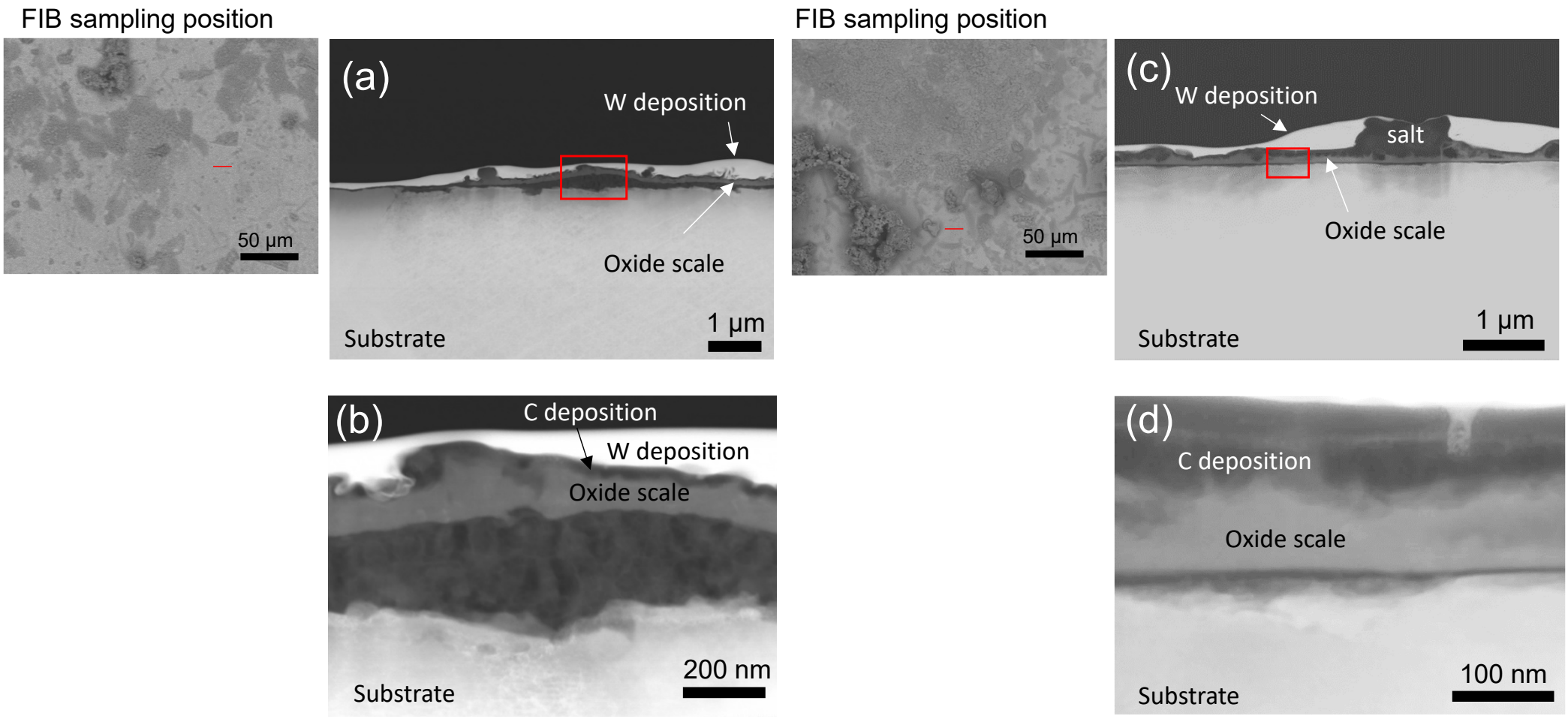


Fig. 6 STEM images after 12 h of corrosion: (a) and (b) SUS310S, (c) and (d) QSX5

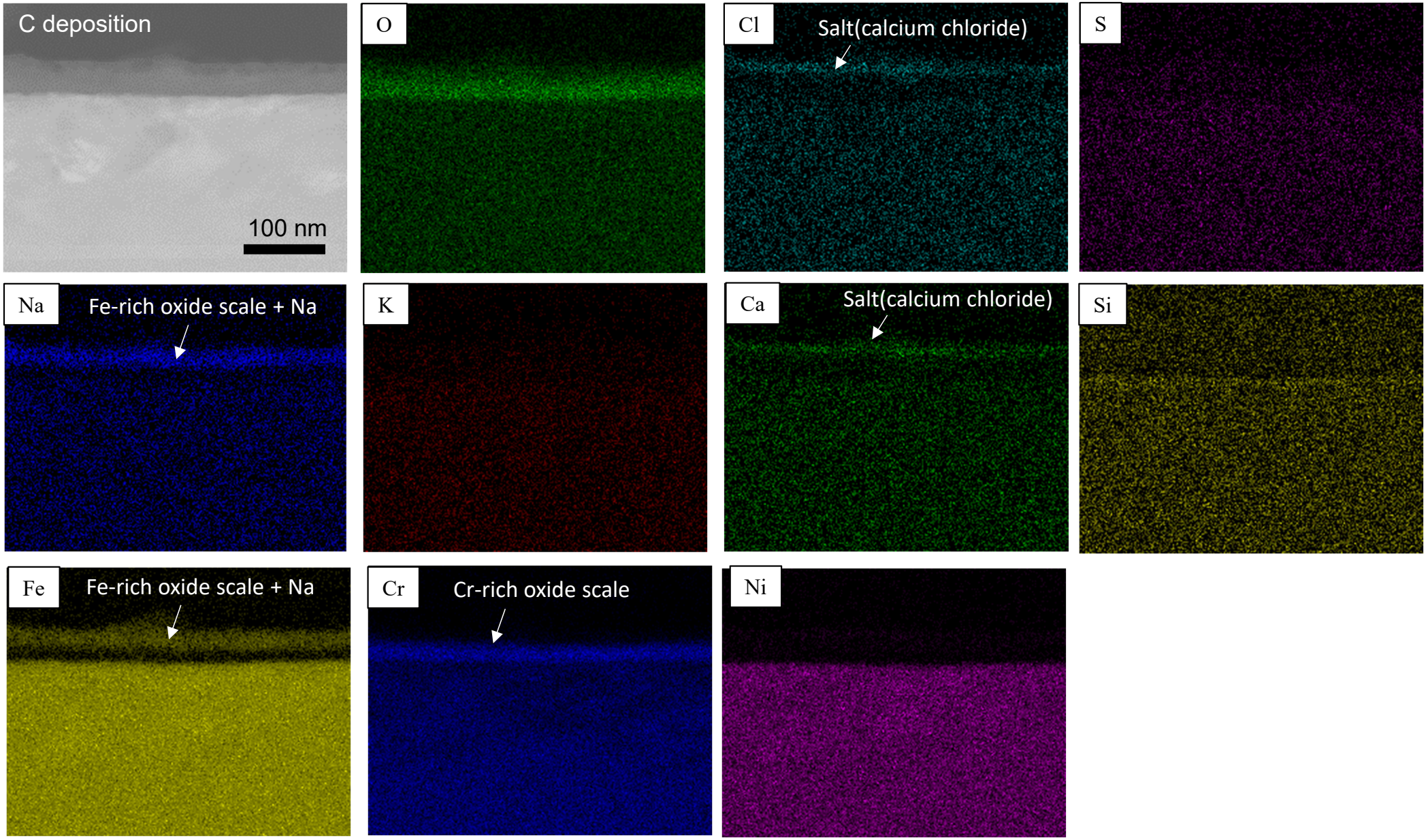


Fig. 7 Elemental distribution maps of SUS310S after 1 h of corrosion

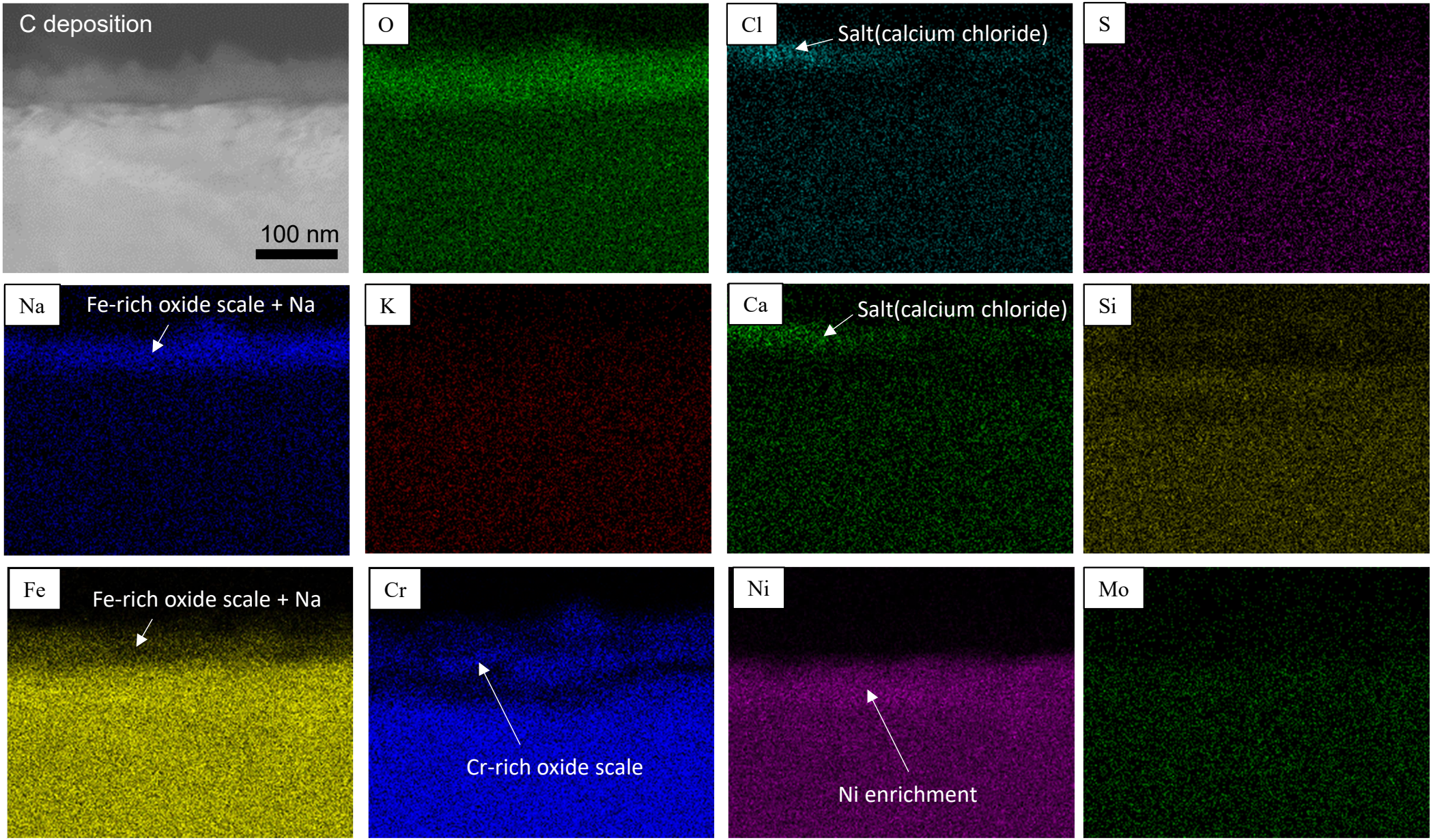


Fig. 8 Elemental distribution maps of QSX5 after 1 h of corrosion

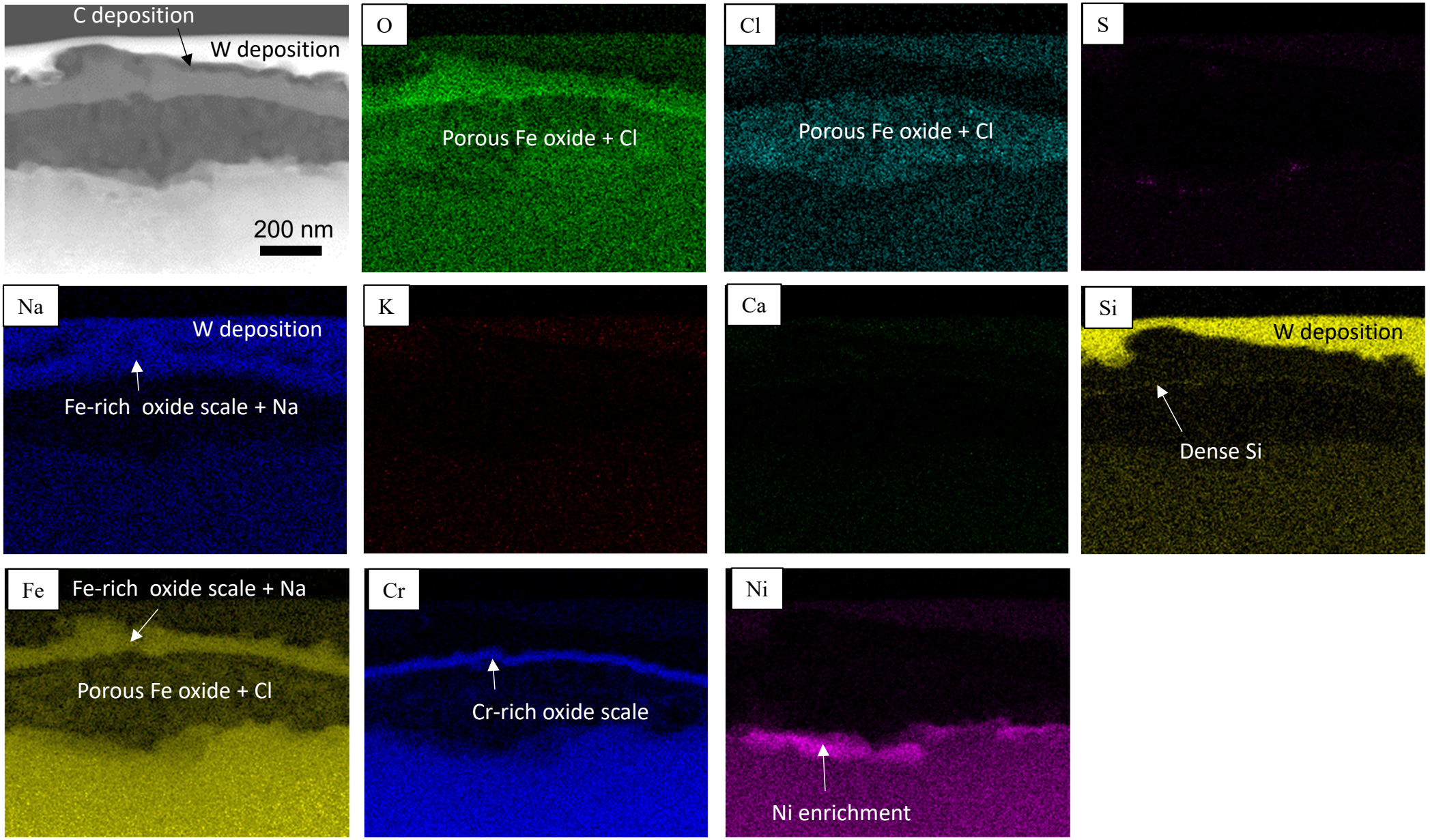


Fig. 9 Elemental distribution maps of SUS310S after 12 h of corrosion

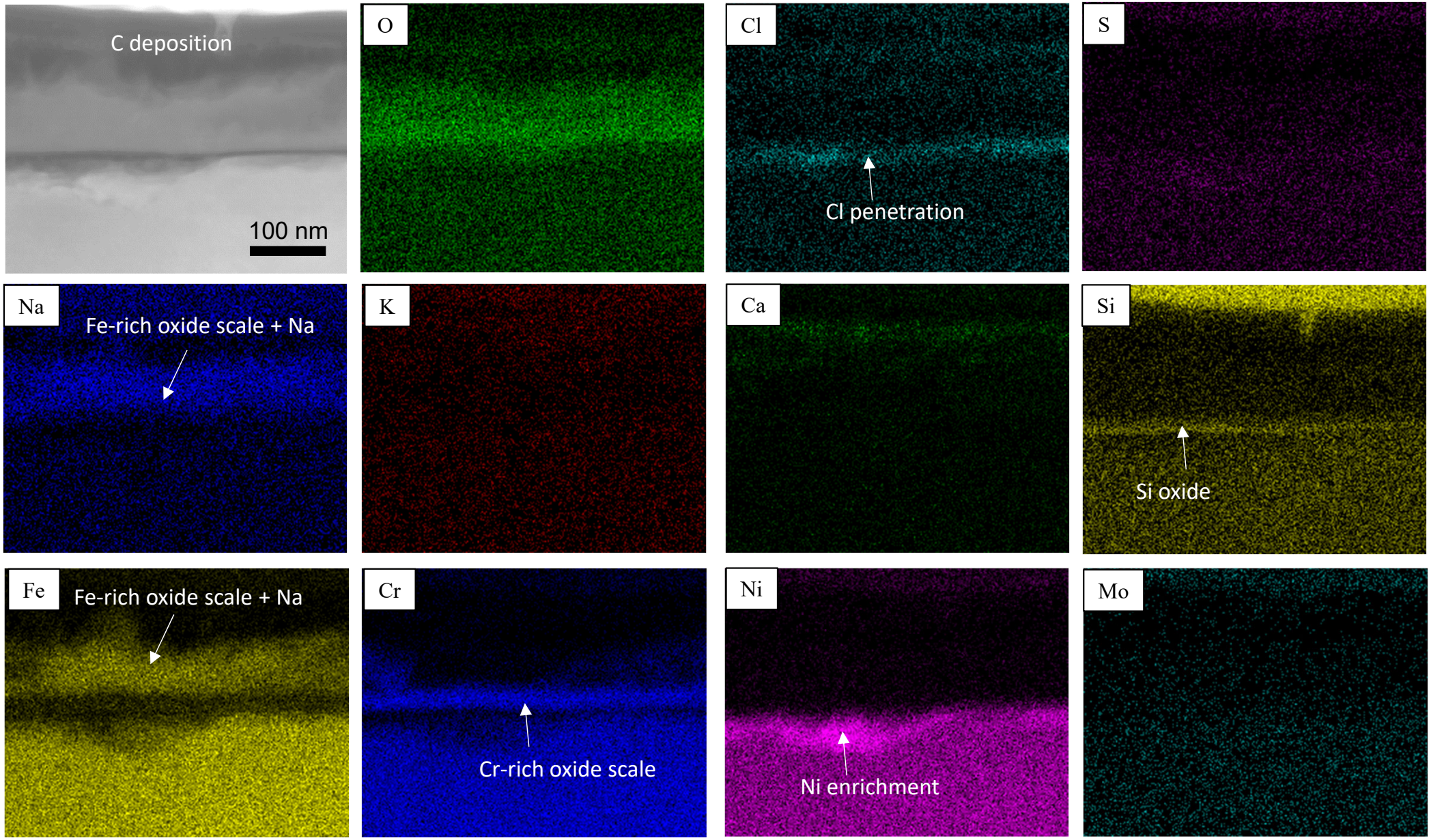


Fig. 10 Elemental distribution maps of QSX5 after temperature gradient corrosion test for 12 h

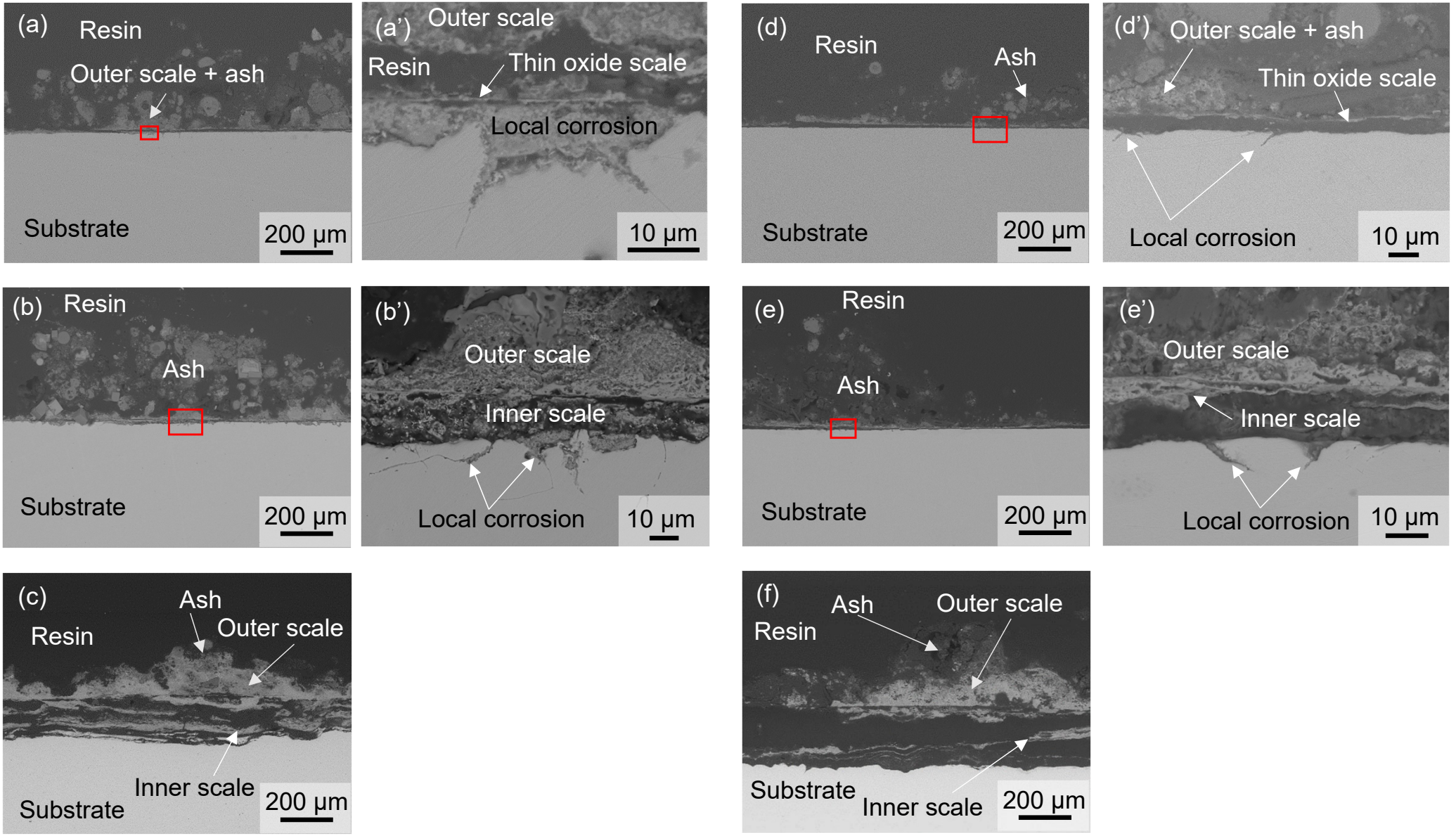


Fig. 11 Cross-sections after the corrosion tests:
(a) and (a') SUS310S for 24 h, (b) and (b') SUS310S for 60 h, (c) SUS310S for 100 h,
(d) and (d') QSX5 for 24 h, (e) and (e') QSX5 for 60 h, and (f) QSX5 for 100 h

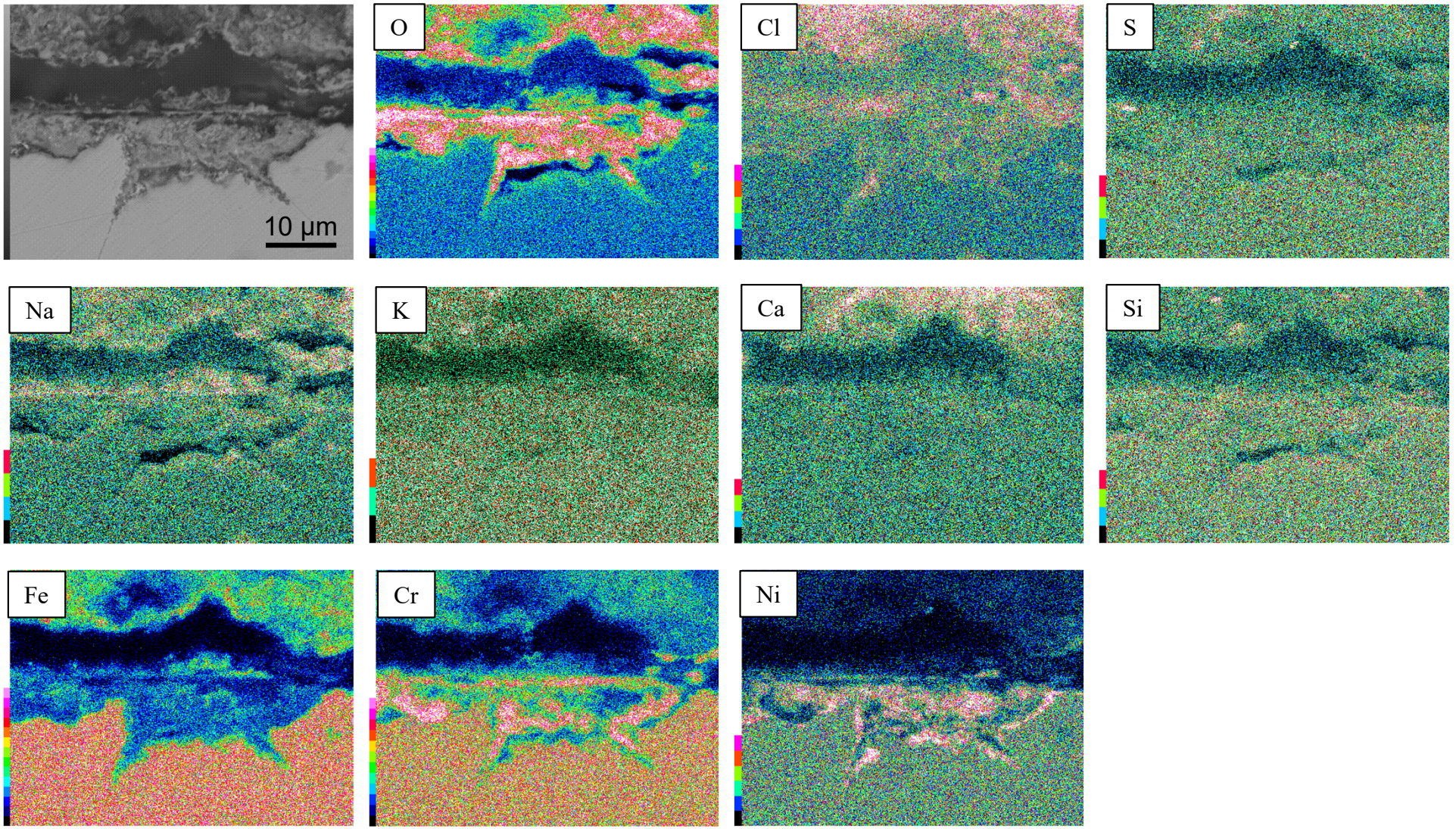


Fig. 12 Elemental distribution maps of SUS310S after 24 h of corrosion

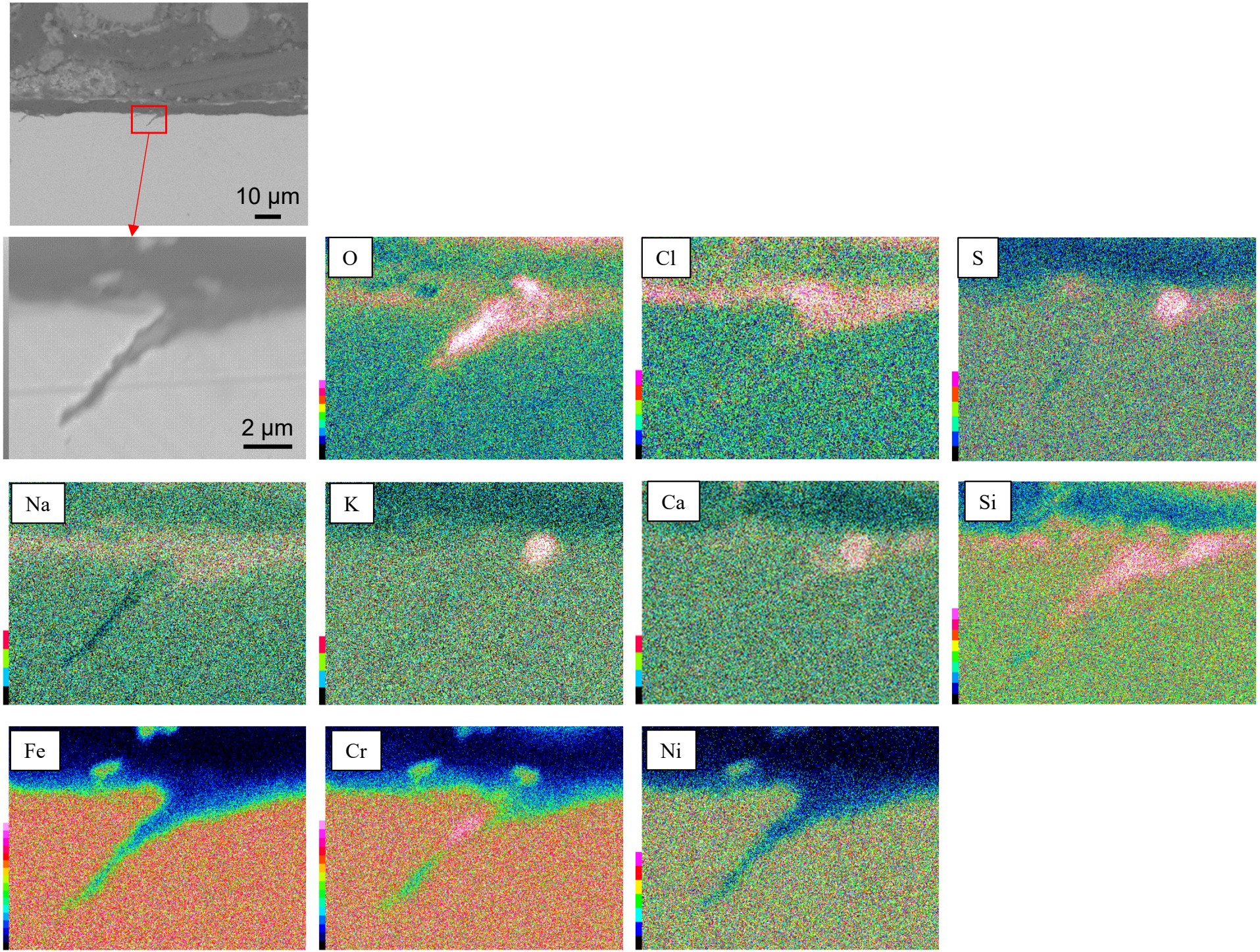


Fig. 13 Elemental distribution maps of QSX5 after 24 h of corrosion

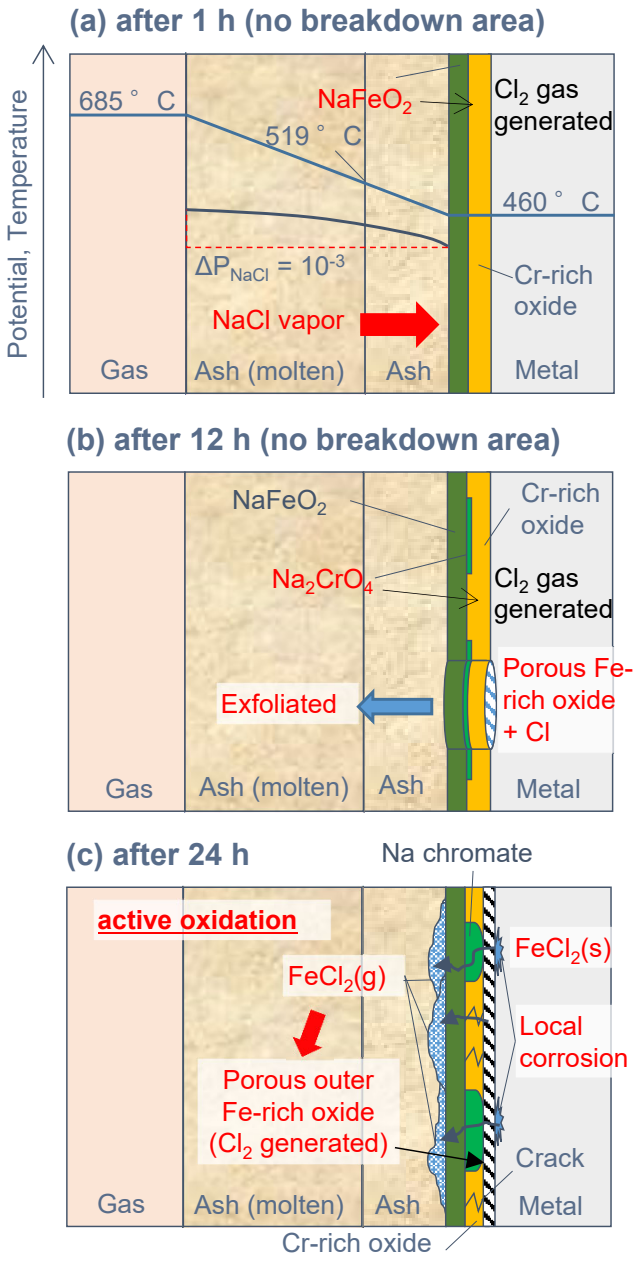


Fig. 14 Schematic image of corrosion behavior before the breakdown of protective Cr-rich oxide scale

Table 1 Chemical compositions of the superheater tube materials (nominal in mass %)

	Si	**Mo**	**N**	**Cr**	**Ni**	**Fe**
SUS310S	≦1.50	—	—	24.0～26.0	19.0～22.0	Bal.
QSX5	2.50～3.50	1.00～2.00	0.042	24.0～26.0	22.0～25.0	Bal.

Table 2 Tube side ash composition determined by XRF (in mass%)

	Ca	O	Cl	K	Si	S	Na	Al	Ti	Fe	Mg	Zn	C	Pb
tube side	20.7	19.0	31.3	9.5	1.8	2.9	9.6	1.5	0.7	0.5	0.7	0.6	0.0	0.05

Table 3 Chemical treatment procedure based on ISO 17428:2015(E)

	Chemical agents	**Time (min)**	**Temperature**
Step 1	90 g of sodium hydroxide (NaOH) 15 g of potassium permanganate ($KMnO_4$) distilled water to make 500 ml	30	Boiling
Step 2	50 g ammonium citrate ($(NH_4)_2C_2H_6O_7$) distilled water to make 500 ml	30	Boiling